Journal of Rock Mechanics and Geotechnical Engineering 16 (2024) 1245–1261

Contents lists available at ScienceDirect

Journal of Rock Mechanics and Geotechnical Engineering

journal homepage: www.jrmge.cn

Full Length Article

Mechanical behaviours of bedded sandstone under hydromechanical coupling

Junwen Zhang [a], Zhixiang Song [a,*], Lichao Zhang [b], Shaokang Wu [a], Shanyong Wang [c], Yang Zhang [a], Xukai Dong [a], Jinxin Wang [a], Yanbo Han [a], Baohua Kan [a]

[a] School of Energy and Mining Engineering, China University of Mining and Technology (Beijing), Beijing, 100083, China
[b] Jarud Banner Zhahanao'er Coal Industry Co., Ltd., Zhaluteqi, Inner Mongolia, 029200, China
[c] Priority Research Centre for Geotechnical Science & Engineering, The University of Newcastle, Callaghan, NSW 2308, Australia

ARTICLE INFO

Article history:
Received 26 February 2023
Received in revised form
17 August 2023
Accepted 19 October 2023
Available online 23 January 2024

Keywords:
Hydromechanical coupling
Bedded sandstones
Mechanical behaviour
Bedding effect
Failure mechanism

ABSTRACT

The combination of the dipping effect and hydromechanical (H-M) coupling effect can easily lead to water inrush disasters in water-rich roadways with different dip angles in coal mines. Therefore, H-M coupling tests of bedded sandstones under identical osmotic pressure and various confining pressures were conducted. Then, the evolution curves of stress-strain, permeability and damage, macro- and mesoscopic failure characteristics were obtained. Subsequently, the mechanical behaviour was characterized, and finally the failure mechanism was revealed. The results showed that: (1) The failure of the sandstone with the bedding angle of 45° or 60° was the structure-dominant type, while that with the bedding angle of 0°, 30° or 90° was the force-dominant type. (2) When the bedding angle was in the range of (0°, 30°) or (45°, 90°), the confining pressure played a dominant role in influencing the peak strength. However, within $\beta \in (30°, 45°)$, the bedding effect played a dominant role in the peak strength. (3) With the increase in bedding angle, the cohesion increased first, then decreased and finally increased, while the internal friction angle was the opposite. (4) When the bedding angle was 0° or 30°, the "water wedging" effect and the "bedding buckling" effect would lead to the forking or converging shear failure. When the bedding angle was 45° or 60°, the sliding friction effect would lead to the shear slipping failure. When the bedding angle was 90°, the combination of the "bedding buckling" effect and shear effect would lead to the mixed tension-shear failure. The above conclusions obtained are helpful for the prevention of water inrush disasters in water-rich roadways with different dips in coal mines.
© 2024 Institute of Rock and Soil Mechanics, Chinese Academy of Sciences. Production and hosting by Elsevier B.V. This is an open access article under the CC BY-NC-ND license (http://creativecommons.org/licenses/by-nc-nd/4.0/).

1. Introduction

Accurate and effective characterization of rock mechanical behaviour under the H-M effect is a key scientific issue in geotechnical engineering, including the deformation, strength, permeability, damage and mesoscale failure. Among them, crack initiation, propagation and coalescence, and even the formation of a shear zone, are related to the mechanical behaviours described above. Additionally, there are numerous microstructures, single joint and multiple joints, where several "isolated islands" of water and even gas are stored in the deep strata at a certain depth (Zhang et al., 2021; Song et al., 2023a). Due to the variability of geological structures, there are different layouts of water-rich roadways with different dip angles in coal mines. The combination of the dipping effect and H-M coupling effect can easily lead to a series of water inrush disasters in the water-rich roadways with different dip angles of coal mines. Furthermore, sandstone, as a commonly buried geological material, is the research object for conducting mechanics tests (Maruvanchery and Kim, 2020; Su and Liu, 2020; Kang, 2021; Zhang et al., 2021; Song and Zhang, 2022). Hence, it is urgent to systematically conduct researches on the mechanical behaviours of bedded sandstone under H-M coupling, which could provide the theoretical references for the prevention of water inrush disasters in water-rich roadways with different dips in coal mines.

To date, numerous studies on the mechanical behaviours of coal and rocks under H-M coupling have been conducted, and relatively abundant research achievements have also been obtained. On the one hand, under the action of high in situ stress, the mechanical behaviours of coal reservoirs containing water occurred can be

* Corresponding author.
E-mail address: szxcumtb@126.com (Z. Song).
Peer review under responsibility of Institute of Rock and Soil Mechanics, Chinese Academy of Sciences.

https://doi.org/10.1016/j.jrmge.2023.10.016
1674-7755 © 2024 Institute of Rock and Soil Mechanics, Chinese Academy of Sciences. Production and hosting by Elsevier B.V. This is an open access article under the CC BY-NC-ND license (http://creativecommons.org/licenses/by-nc-nd/4.0/).

significantly affected. Therefore, related studies on the mechanical behaviour of coal under H-M coupling have been conducted by former experts. Among them, it has been verified that water can significantly weaken the bearing strength of coal (Perera et al., 2011; Poulsen et al., 2014; Vishal et al., 2015). Additionally, water can not only change the pore structure of coal but also significantly affect its deformation and permeability properties (Han et al., 2010; Pan et al., 2010; Wang et al., 2011; Chen et al., 2013; Ren et al., 2020). Furthermore, a series of permeability models of coal has been built considering the H-M coupling effects (Izadi et al., 2011; Zhu and Wei, 2011; Chen et al., 2012). For example, a permeability evolution model of coal considering the elasto-plastic deformation stages under H-M coupling was proposed (Wang et al., 2022). Additionally, a novel coupled H-M model considering subsidence during the gas extraction of coal seams was also established (Wu et al., 2019). On the other hand, H-M coupled processes of rock masses with various lithologies are also significant in rock engineering, including oil and gas engineering, slope engineering, underground engineering, and nuclear waste disposal. Therefore, scholars worldwide have conducted related studies on the mechanical behaviours of rock masses with various lithologies under H-M coupling, and relatively abundant research achievements have been obtained (Wang et al., 2009; Watanabe et al., 2010; Morris et al., 2011; Rutqvist et al., 2011; Lei et al., 2015; Zhou et al., 2023). Yan et al. (2023) characterized the mechanical behaviours of prefabricated jointed granite with different dip angles under H-M coupling, and proposed a damage constitutive model. Jiang et al. (2012) explored the mechanical behaviours of a fractured rock mass under H-M coupling with a high water pressure of 7.8 MPa. Nguyen et al. (2018) modelled the short- and long-term hydromechanical behaviours of argillaceous limestone, including the deformation and permeability behaviours. Additionally, the mechanical behaviours of other rocks with different lithologies have been previously investigated (Le and Nguyen, 2015; Hu et al., 2017; Li et al., 2017; Ng and Carlos Santamarina, 2023; Zheng et al., 2022). The findings reported in the above studies have made significant progress in understanding the H-M coupled mechanical behaviours of rocks with various lithologies. A solid knowledge of the mechanical behaviour evolution characteristics of coal or rocks under H-M coupling is crucial for stability control in geotechnical engineering. Nevertheless, few studies have been performed on the failure mechanism while considering the bedding effect of coal or rocks under H-M coupling. Therefore, the failure mechanism considering the bedding effect of coal or rocks under H-M coupling is worthy of further research.

The above studies have mainly been focused on the characterization of the H-M coupled mechanical behaviours of coal and rocks without consideration of the bedding effect. Furthermore, most investigations have been limited to H-M coupled mechanical behaviours of bedded coal or bedded rocks with horizontal or vertical bedding angle, but those under other inclination angles, such as 30°, 45° and 60°, have often been ignored. Therefore, it is urgent to systematically study the bedding effect on the mechanical behaviours of sandstone under H-M coupling.

First, H-M coupling experiments under different bedding angles (0°, 30°, 45°, 60° and 90°), identical osmotic pressure (4 MPa) and various confining pressures (10 MPa, 20 MPa and 30 MPa) were conducted. Subsequently, the evolutions of stress-strain, permeability and damage, macro- and microscopic failure characteristics were obtained. Finally, based on the strength, deformation, macro- and microfracture characteristics, damage evolution law and permeability evolution characteristics, the failure mechanism of bedded sandstone with different bedding angles under H-M coupling was revealed.

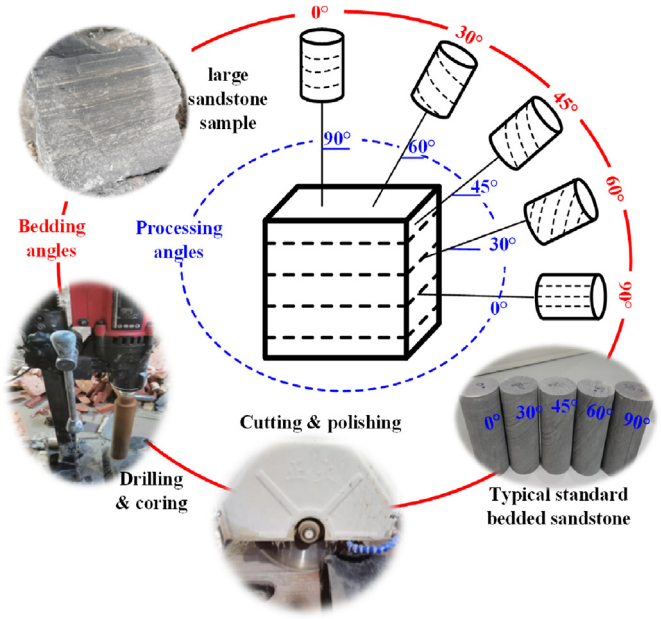

Fig. 1. Processing scheme.

2. Test preparation and scheme

2.1. Test materials

A detailed introduction to the sampling and preparation of rock samples can be found in Song et al. (2023a). Among them, the general situations of rock samples are described as follows: (i) The dense bedded structures are evenly distributed; (ii) The bedding is significant; and (iii) The colour is greyish-black. As shown in Fig. 1, the diameter and height of cylindrical specimens processed with various bedding angles are 50 mm and 100 mm, respectively.

Additionally, the TOP INDUSTRIE Rock 600-50 multifield coupling testing system was used in the tests (see Fig. 2a), and the corresponding functional details are shown in Table 1.

2.2. Set loadings, test assistance and preparation

To obtain the mechanical behaviours of bedded sandstone under H-M coupling, the H-M experiment scheme of bedded sandstones was designed. The specific details are described as follows:

(1) Preparations before the tests. To exhaust the air stored in the bedded sandstone and reduce test error, the bedded sandstone was subjected to vacuum water saturation treatment with negative pressure for 24 h.
(2) Acoustic emission (AE) installation and monitoring. The emission probe was arranged on the upper and lower ends of the outer cavity, the two probes were parallel to each other, and the center of the two probes was on the same axis. In addition, the transmitting signal was extracted by a dual-channel method, and the induction frequency of the AE probes was between 10 and 30 kHz.
(3) μCT scanning tests. Finally, μCT scanning tests of the fractured bedded sandstone were conducted to obtain the mesoscopic fracture characteristics after H-M coupling tests.

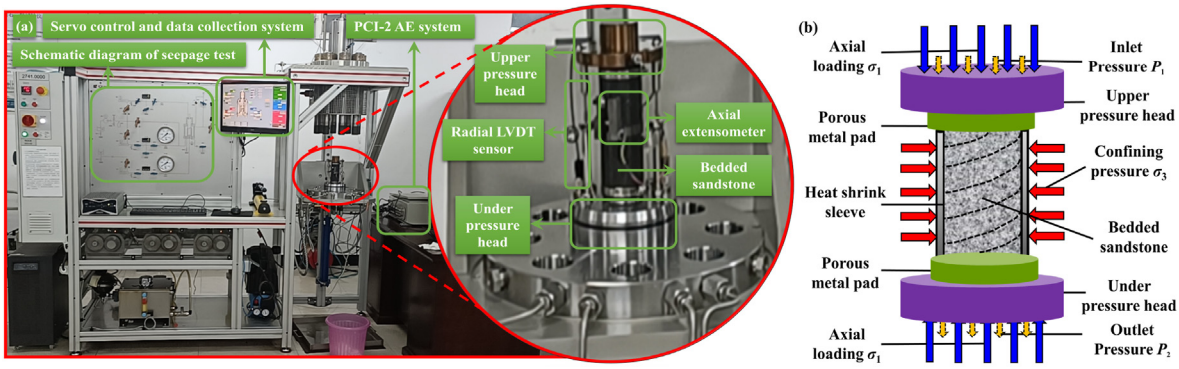

Fig. 2. (a) TOP INDUSTRIE Rock 600-50 multifield coupling testing system and (b) seepage diagram.

2.3. Test schemes

The test schemes for this study are described as follows:

(1) Specimen installation. The installation process needs to ensure the sealing of the heat-shrinkable sleeve and the specimens. Therefore, seepage water can be avoided from the minute gap between the specimens and the heat-shrinkable sleeve as much as possible. Meanwhile, to avoid the phenomenon of oil film blocking the seepage channels, the mixing of silicone oil and water under confining pressure needs to be avoided in the later period. The test device after installation is shown in Fig. 2a.
(2) Set the confining pressure σ_3. After the specimens were installed, a 1 kN axial preload was applied to the specimens for initial fixation. Then, the confining pressure σ_3 was applied to the preset gradient value, and the loading rate was set to 1 MPa/min (see Fig. 3).
(3) Set the osmotic pressure P_g. The osmotic pressure P_g was applied to a preset value of 4 MPa, and the loading rate was also set to 1 MPa/min (among them, the inlet pressure P_1 and the outlet pressure P_2 were kept at constant values of 4 MPa and 0 MPa, respectively, see Fig. 2b).
(4) Set the axial pressure σ_1. The continuous axial loading σ_1 was set on the bedded sandstone. Among them, a displacement control mode was adopted, and the loading rate was set at 0.06 mm/min. Then, the loading was stopped until the post-peak residual stage occurred. In the whole process, the dynamic permeability was measured every 10 MPa and the corresponding seepage principle is shown in Fig. 2b. Meanwhile, the system automatically recorded and saved the relevant data.

The steady-state method was adopted in the tests to measure the dynamic permeability, and the corresponding dynamic permeability was calculated as follows (Zhao et al., 2021; Yu et al., 2022):

$$k_i = \frac{\mu L \Delta Q_i}{A P_g \Delta t_i} \tag{1}$$

where k_i is the average permeability during the time Δt_i (m^2); μ is the fluid viscous coefficient, $\mu = 100.5 \times 10^{-5}$ Pa s; ΔQ_i is the seepage volume during the time Δt_i (m^3); L is the height of the deep bedded sandstone (m); A is the cross-sectional area of the deep bedded sandstone (m^2); P_g is the osmotic pressure ($P_g = P_1 - P_2$, P_1 is the inlet pressure, P_2 is the outlet pressure); and Δt_i is the time interval between recording points (s).

3. Results and discussion

3.1. Stress–strain and macroscopic failure types

There were four macroscopic failure types under H-M coupling (see Fig. 4), i.e. type ① - shear failure through the bedding plane, type ② - shear failure along the bedding plane, type ③ - shear failure half-along the bedding plane, and type ④ - mixed tension-shear failure.

When the bedding angles were 0° and 30°, the macroscopic failure mode belonged to the type ①. The fracture angle was relatively large under low confining pressure. Meanwhile, the shear failure type was significant, and the local deformation developed in the perpendicular direction. The fracture angle gradually decreased with the increase in confining pressure.

The macroscopic failure types with the bedding angle of 45° were mainly types ② and ③. And the cracking direction of the macroscopic failure surfaces was basically the same as that of the weak bedding plane of 45°, which indicated that the weak planes with inclination angle of 45° could significantly induce and accelerate the emergence of the macroscopic failure surfaces. The fracture angle of the macroscopic failure surfaces was basically the same as the increase of confining pressure, which indicated that the confining pressure had little effect on the macroscopic failure type of bedded sandstone with a bedding angle of 45°.

The macroscopic failure type of the specimen with the bedding angle of 60° was type ②. The cracking direction of macroscopic failure surfaces was basically identical with that of the weak bedding plane of 60°, which indicated that the weak bedding plane of 60° could also significantly induce and accelerate the emergence of the macroscopic failure plane. Meanwhile, the fracture angle of the macroscopic failure surfaces was also basically the same as the increase of confining pressure. It was indicated that the confining pressure had little effect on the macroscopic failure type of the specimen with the weak bedding plane of 60°.

The macroscopic failure types of the specimen with the bedding angle of 90° were types ① and ④. Because the bedding angle of 90° was parallel to the loading direction of axial stress and perpendicular to the loading direction of the confining pressure, the macroscopic local tensile cracks in vertical direction had the obvious inducing effect. Meanwhile, the accompanying local shear fracture characteristics were mainly attributed to the action of effective stresses.

In conclusion, the macroscopic failure type was closely connected with the weak plane structures and effective stresses. The evolution process of the failure types with increasing bedding angle was as follows: type ① → type ③ → type ② → type ④. Each type of macroscopic failure was affected by the bedding structures.

Table 1
Functions of the TOP INDUSTRIE Rock 600-50 multifield coupling testing system.

Test equipment	Performance indicator	Main function	Advantage
TOP INDUSTRIE Rock 600-50 multifield coupling testing system	The threshold of axial pressure is 300 MPa; the threshold of confining pressure is 60 MPa; the threshold of temperature is 200 °C	Uniaxial compression or Brazilian splitting or creep or relaxation tests; Triaxial loading or cyclic loading and unloading tests; Hydromechanical coupling test	It can realize long-term high-load operation; the pressure and temperature thresholds can meet the relevant conditions of rock mechanics; it has high precision and modularity

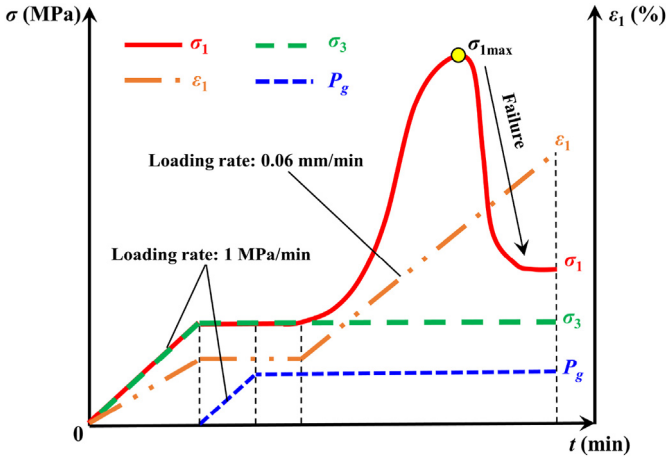

Fig. 3. Loading path of the H-M coupling test (Song et al., 2023b).

Meanwhile, the fundamental differences relied on the stress direction and the bedding structures with different angles under H-M coupling. However, the test results indicated that the bedding effect that affected the failure behaviour was relatively low (brittle failure induced by the vertical stress and the failure plane is predominantly subvertical) of bedded sandstone.

In terms of the hydraulic effect, as shown in Figs. 4b and 5, the peak deviatoric stress with identical bedding angle under H-M coupling was weaker than that under the single stress field condition, and the hydromechanical coupling effect was significant. Meanwhile, the radial and axial deformation resistances of bedded sandstone under the single stress field were obviously weaker than that under H-M coupling. Therefore, the hydromechanical coupling effect can not only reduce the bearing capacity, but also strengthen its deformation resistance.

As shown in Fig. 6, the fracture angle of the specimen with the bedding angle of 30° or 90° under the single stress field was obviously larger than that under H-M coupling. In contrast, the fracture angle of the specimen with the bedding angle of 0°, 45° or 60° under the single stress field was significantly greater than that under H-M coupling. It was suggested that both bedding angle and hydromechanical coupling effect can significantly influence the evolution characteristics of the fracture angle. Furthermore, the fracture angle with identical bedding angle under H-M coupling decreased with the increase in confining pressure.

3.2. Mesoscopic failure characteristics

To accurately obtain the mesoscopic failure types under H-M coupling, it is necessary to systematically conduct the corresponding μCT scanning tests. Therefore, the front, left, vertical views and three-dimensional (3D) reconstruction of the fractured bedded sandstone under different working conditions were obtained. The corresponding details are shown in Fig. 7 and Table 2.

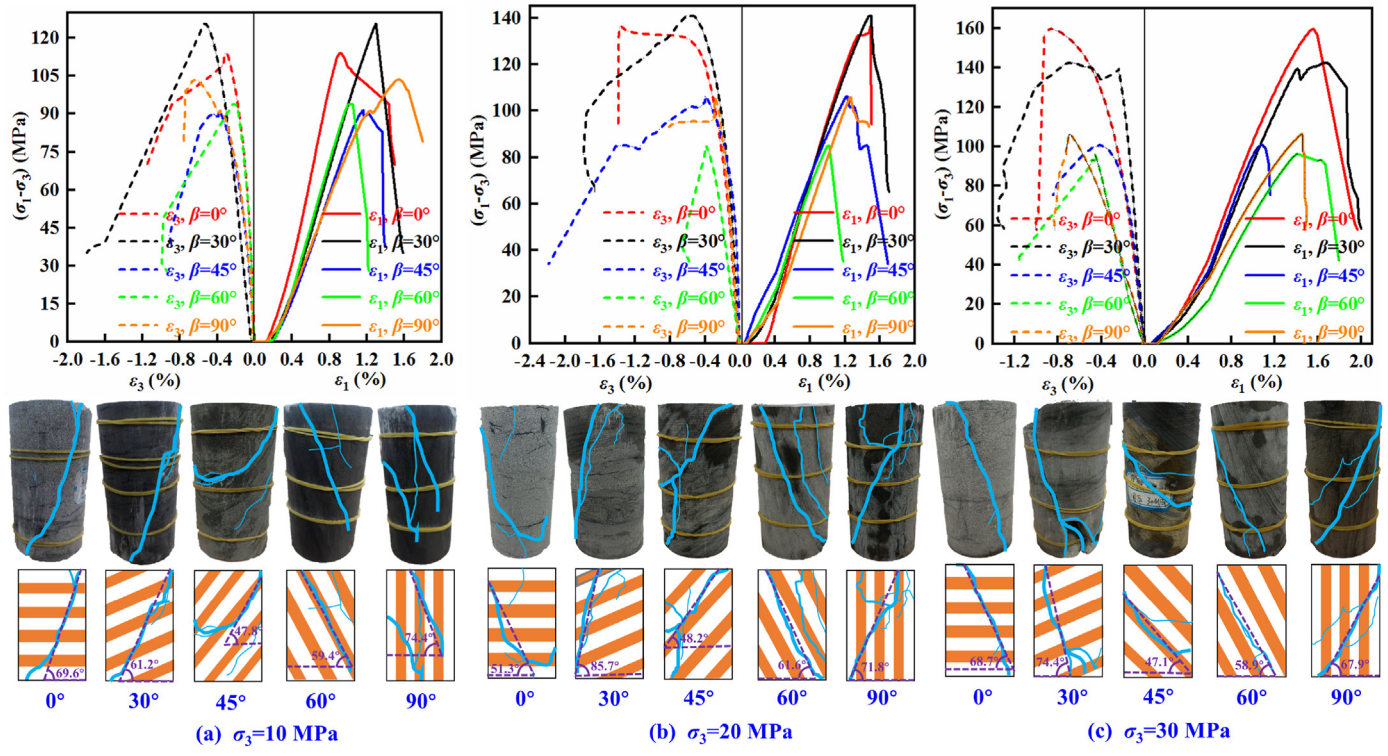

Fig. 4. Stress–strain curves and macroscopic failure characteristics under H-M coupling (P_g = 4 MPa) (Song et al., 2023b).

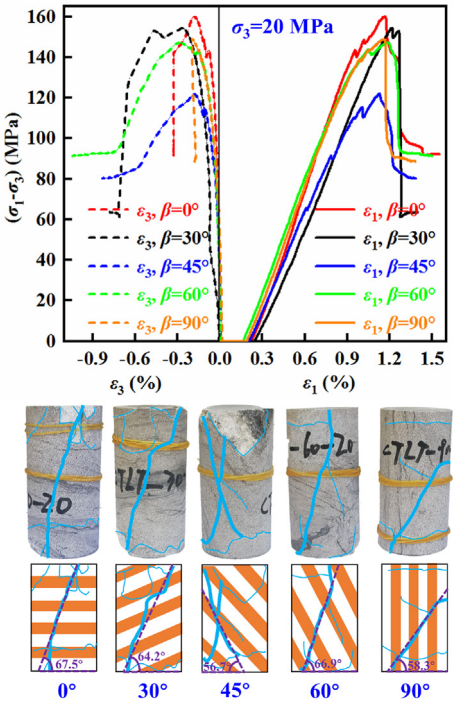

Fig. 5. Stress–strain curves and macroscopic failure characteristics under single stress field (Song et al., 2023c).

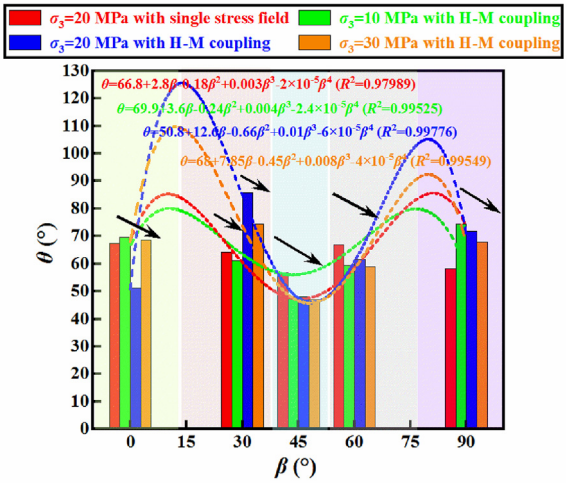

Fig. 6. The fracture angle θ under H-M coupling and a single stress field.

Similarly, there were two main mesoscopic failure types, i.e. type I - shear failure through the bedding plane and type II - shear failure half-through the bedding plane. However, there were mesoscopic failure patterns with different shapes, such as “Y"-shape, “Tree"-shape, "π"-shape, "/"-shape, "//"-shape and "///"-shape.

There were significant differences in the mesoscopic failure types under identical bedding angle and various confining pressures. In the through form of the mesoscopic failure types, the bedded sandstone under low and middle confining pressures all showed the mesoscopic failure of type I, while that under high confining pressure all showed the mesoscopic failure of type II, and the fracture surface was relatively single. This is due to the existence of high confining pressure, which significantly inhibited the

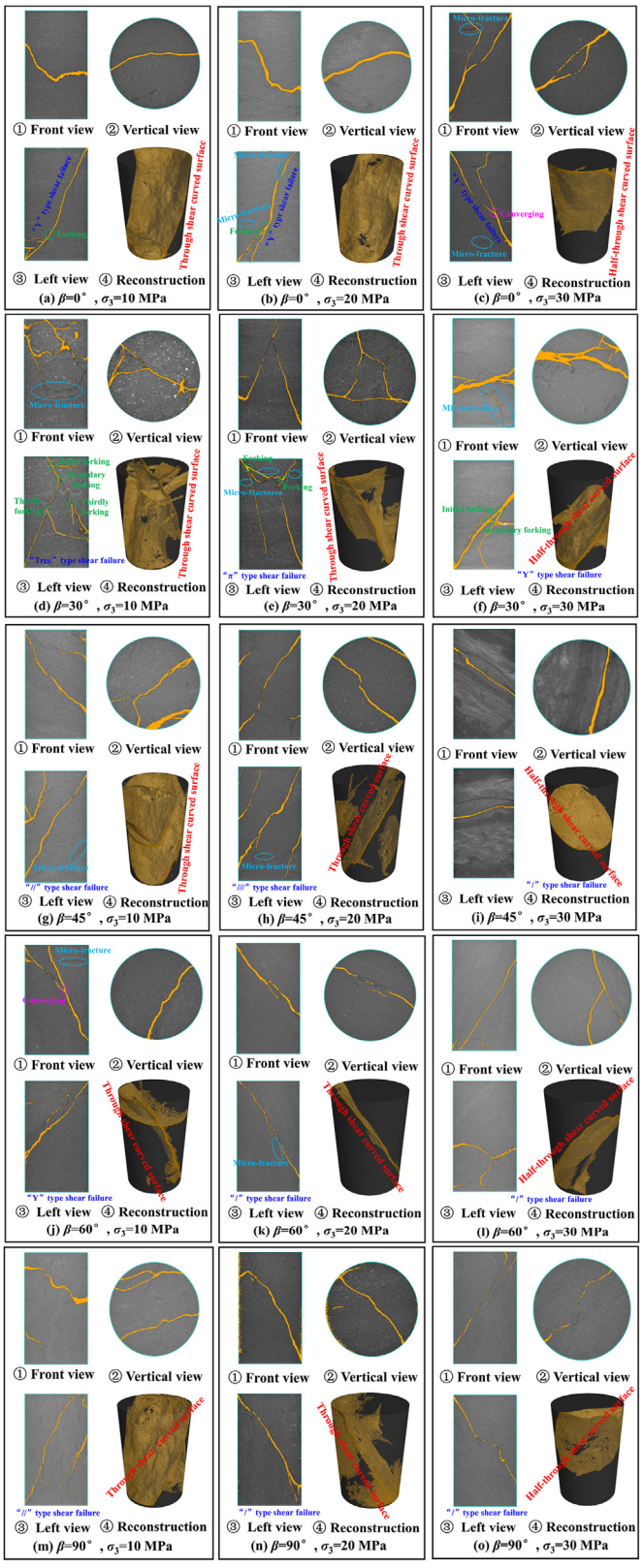

Fig. 7. Mesoscopic failure characteristics under H-M coupling.

derivation and propagation of the radial tension cracks. Meanwhile, the high effective stress can not only improve the selection ability of the internal dominant seepage channels, but also greatly

Table 2
Marco- and mesoscopic failure characteristics and type determination under H-M coupling.

β (°)	σ_3 (MPa)	Macroscopic failure type	Mesoscopic failure type	Subordination type
0	10	Type ①	Type I with "Y"-shape	Force-dominant
	20	Type ①	Type I with "Y"-shape forking	Force-dominant
	30	Type ①	Type II with "Y"-shape converging	Force-dominant
30	10	Type ①	Type I with "Tree"-shape multivariate and multilevel forking	Force-dominant
	20	Type ①	Type I with "π"-shape multivariate forking	Force-dominant
	30	Type ①	Type II with "Y"-shape multilevel forking	Force-dominant
45	10	Type ②	Type I with "//"-shape	Structure-dominant
	20	Type ③	Type I with "///"-shape	Structure-dominant
	30	Type ③	Type II with "/"-shape	Structure-dominant
60	10	Type ②	Type I with "Y"-shape converging	Structure-dominant
	20	Type ②	Type I with "/"-shape	Structure-dominant
	30	Type ②	Type II with "/"-shape	Structure-dominant
90	10	Type ④	Type I with "//"-shape	Force-dominant
	20	Type ④	Type I with "/"-shape	Force-dominant
	30	Type ①	Type II with "/"-shape	Force-dominant

improve the bearing capacity and the overall stiffness of bedded sandstone. Therefore, the bedded sandstones under high confining pressure can form the characteristics of shear fracture half-through the bedding plane. Although there were similar mesoscopic failure types under identical bedding angle and various confining pressures, there were eight mesoscopic failure types in the mechanical behaviour of mesoscopic failure from the top-down seepage direction.

The significant shear slipping facture along the bedding plane was formed under bedding angles of 45° and 60°. It is noted that the bedding structures played a leading role in influencing the failure mode. Therefore, their failure type was the structure-dominant type. However, the shear failure through the bedding plane or compound failure was demonstrated under bedding angles of 0°, 30° and 90°. It is indicated that external loads played a leading role in influencing the failure mode. Therefore, the corresponding failure type was considered to be a force-dominated type.

There were two types of mesoscopic failure surfaces in bedded sandstone under different working conditions: half-through type and fully-through type. However, it was not difficult to find that the mesoscopic failure surfaces after 3D reconstruction were smooth. Therefore, there was no accumulation or blockage of broken particles. This was due to the comprehensive actions of axial pressure and effective confining pressure, which resulted in continuous extrusion deformation and secondary crushing of the broken particles in the fracture surface of bedded sandstone, thus effectively reducing their particle size and volume. Therefore, in this process, the continuous scouring of seepage water could effectively carry away the particles after secondary fragmentation.

In the above mesoscopic failure characteristics, the formation of the main failure surface was mainly caused by the coupling of axial pressure, confining pressure and bedding structures. However, the derived secondary microscopic cracks were caused by the comprehensive actions of osmotic pressure and bedding structures.

3.3. Anisotropy of strength and deformation

To further clarify the anisotropy evolution law of the peak deviatoric stress and peak strain under H-M coupling, the corresponding details are summarized according to Fig. 4 (see Table 3). The corresponding evolution is shown in Fig. 8.

The peak deviatoric stress under identical bedding angle increased with the increase in confining pressure (see Fig. 8a). When the bedding angle was in the ranges of (0°, 30°) and (45°, 90°), the anisotropy of the peak deviatoric stress gradually strengthened with increasing confining pressure. Hence, the confining pressure played a more dominant role in influencing the peak deviatoric stress than the bedding angle. Nevertheless, when the bedding angle was in the ranges of (30°, 45°), the anisotropy of peak deviatoric stress was basically consistent no matter whether the confining pressure changed. That is, when $\beta \in (30°, 45°)$, the bedding effect played a more dominant role in influencing the peak deviatoric stress than the confining pressure effect.

The confining pressure and bedding significantly influenced the peak axial and radial deformation characteristics under H-M coupling (see Fig. 8b and c). With the increase in confining pressure, the peak axial strain under bedding angles of 0°, 30° and 60° increased, while the corresponding peak radial strain decreased. However, the peak axial and radial strains of the specimen with the bedding angle of 45° did not obviously change with the increase in confining pressure. This indicated that the confining pressure had no obvious effects on the deformation for the specimen with the bedding angle of 45°.

3.4. Strength parameters

To further obtain the strength parameters under H-M coupling, the Mohr stress circles and their envelopes under different effective confining pressures were specifically drawn (see Fig. 9). As shown in Fig. 9, the cohesion and internal friction angle under H-M coupling were obtained (see Table 4 and Fig. 10a).

As shown in Table 4 and Fig. 10a, corresponding to the bedding angles of 0°, 30°, 45°, 60° and 90°, the cohesions C_P of the specimen were 25.7947 MPa, 46.6397 MPa, 39.1187 MPa, 27.7762 MPa and

Table 3
Peak deviatoric stresses and peak strains under H-M coupling.

β (°)	σ_3 (MPa)	P_g (MPa)	σ'_3 (MPa)	$(\sigma_1-\sigma_3)_{cf}$ (MPa)	ε_{1cf} (%)	ε_{3cf} (%)	ε_{Vcf} (%)
0	10	4	6	114.1	0.92	−0.306	0.307
0	20	4	16	136.412	1.308	−0.546	0.215
0	30	4	26	159.667	1.558	−0.869	−0.179
30	10	4	6	125.519	1.3	−0.542	0.215
30	20	4	16	140.984	1.474	−0.521	0.433
30	30	4	26	142.458	1.662	−0.661	0.341
45	10	4	6	91.355	1.164	−0.385	0.395
45	20	4	16	106.3	1.224	−0.401	0.423
45	30	4	26	100.536	1.082	−0.41	0.262
60	10	4	6	93.699	1	−0.21	0.579
60	20	4	16	85.009	1.007	−0.39	0.227
60	30	4	26	96.18	1.413	−0.46	0.493
90	10	4	6	103.617	1.535	−0.629	0.277
90	20	4	16	105.87	1.259	−0.286	0.686
90	30	4	26	106.263	1.454	−0.691	0.073

Note: $(\sigma_1-\sigma_3)_{cf}$ is the peak deviatoric stress; ε_{1cf}, ε_{3cf} and ε_{Vcf} are the axial, radial and volumetric strains corresponding to the peak deviatoric stress, respectively; σ'_3 is the effective confining pressure, and $\sigma'_3 = \sigma_3 - P_g$.

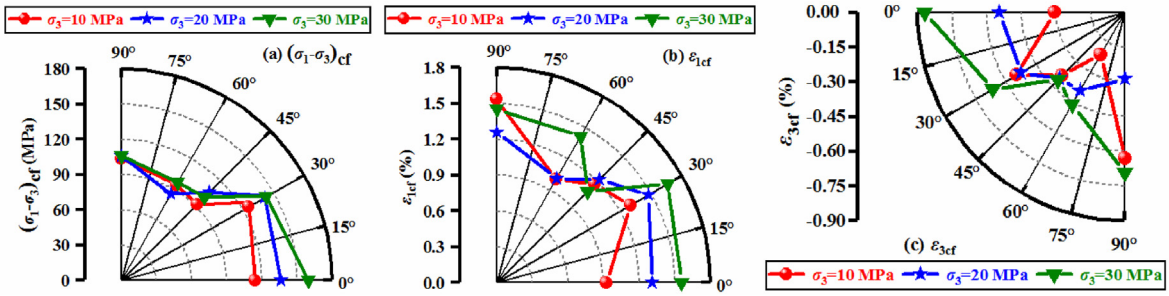

Fig. 8. Anisotropy of the peak deviatoric stress and peak strains under H-M coupling (P_g = 4 MPa) (Song et al., 2023b).

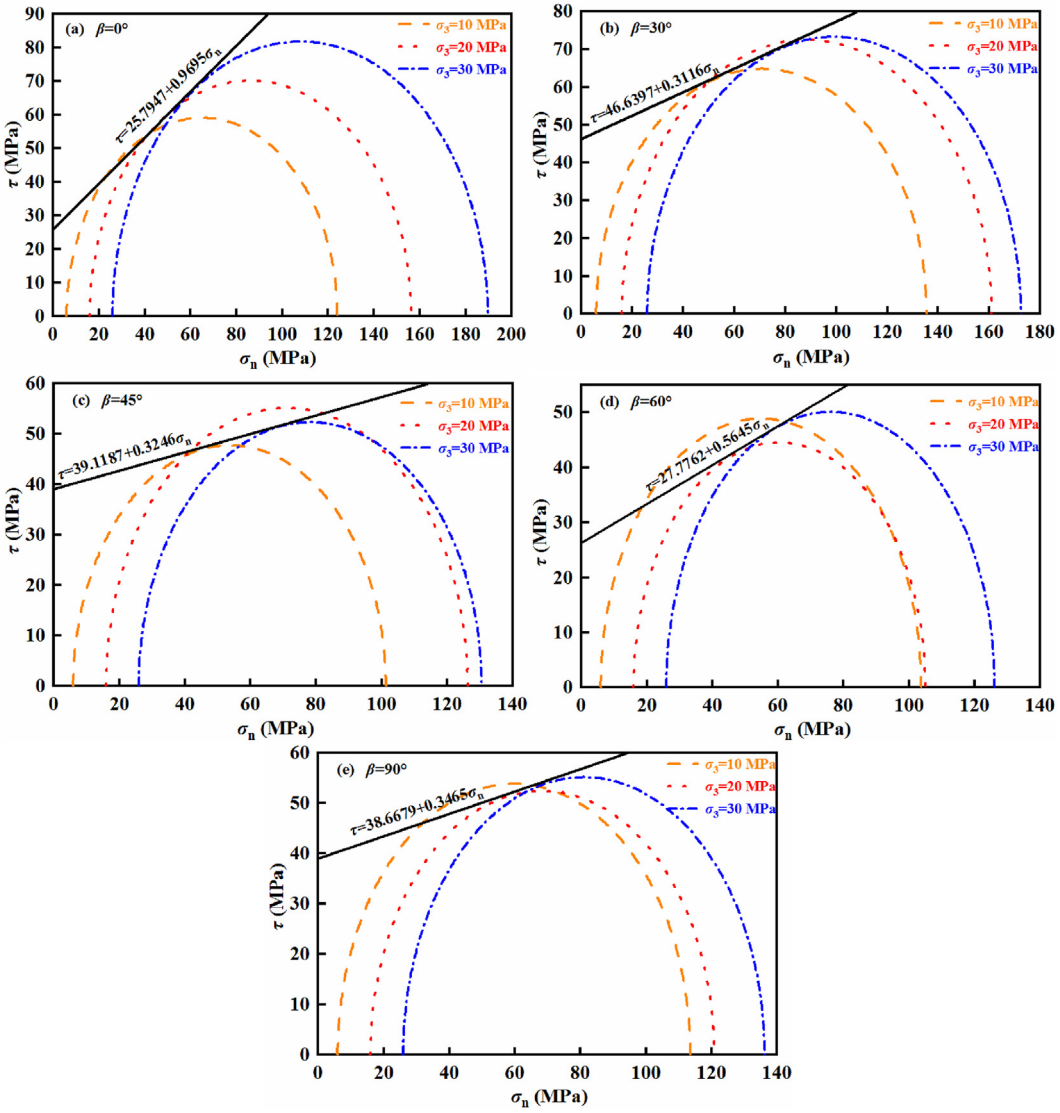

Fig. 9. Mohr stress circles and envelopes under H-M coupling.

38.6679 MPa, and the corresponding internal friction angles φ_P were 44.1123°, 17.3071°, 17.9839°, 29.4466° and 19.1136°, respectively. With increasing bedding angle, the cohesion increased first, then decreased and finally increased, while that of the internal friction angle was the opposite.

Under the comprehensive actions of effective stresses, the whole deformation process of bedded sandstone is essentially the cohesive-weakening-frictional-strengthening process (see Fig. 10b). With the progress of underground excavation, the underground surrounding rocks accompanied by osmotic pressure and bedding continue to experience this process. As a result, the cohesion and internal friction angle of underground surrounding rocks with different bedding angles have significant evolution differences.

Table 4
Cohesion and internal friction angle under H-M coupling.

β (°)	P_g (MPa)	C_P (MPa)	φ_P (°)
0	4	25.7947	44.1123
30	4	46.6397	17.3071
45	4	39.1187	17.9839
60	4	27.7762	29.4466
90	4	38.6679	19.1136

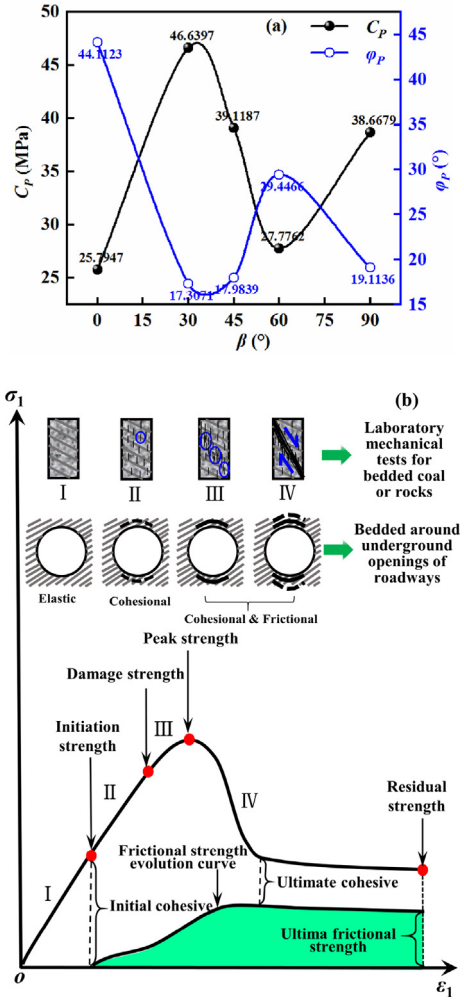

Fig. 10. Cohesion and internal friction angle: (a) Anisotropy, and (b) Cohesive-weakening-frictional-strengthening process with underground excavation engineering (Song et al., 2022).

3.5. Permeability evolution characteristics

To further obtain the permeability evolution characteristics under H-M coupling, the stress-strain-permeability curves are drawn, and one can see that they have similar evolution characteristics (see Fig. 11). Therefore, Fig. 11a is selected to give a representative description for the dynamic permeability evolution law.

At stage I, the stress-strain curve starts to be slightly concave, and its slope gradually increases with increasing load. The reason is that under the initial load, the microcracks of bedded sandstone are gradually compacted, the opening of seepage channels starts to decrease, and the nonlinear deformation is formed. Therefore, the permeability at stage I significantly decreases. Numerically, the initial permeability of 6.302×10^{-5} mD slowly decreases to the minimum permeability of 4.714×10^{-5} mD.

The stress-strain curve at stage II represents the elastic deformation stage. Meanwhile, the opening and number of seepage channels are basically stable, and the permeability is at a low value with slight fluctuations. Numerically, the permeability fluctuates slightly from 4.714×10^{-5} mD to 4.927×10^{-5} mD.

At stage III, the slope of the stress-strain curve begins to decrease at the elastic deformation stage, which gradually enters the stable crack growth stage. At this stage, the internal microcracks begin to derive, expand and develop. Therefore, the number of internal seepage channels increases, and the permeability slowly increases. Numerically, the permeability slowly increases from 4.927×10^{-5} mD to 7.1246×10^{-5} mD.

At stage IV, under the continuous action of axial loads, the bedded sandstone enters the unstable crack growth stage. At this stage, the damage degree is greatly increased. Meanwhile, numerous new cracks can further grow, propagate, coalesce, and nucleate, finally forming the macroscopic shear fracture plane. Therefore, at this stage, the main reason for the sharp increase in permeability is the rapid increase in the number and opening of dominant seepage channels. In addition, the occurrence of the maximum permeability is obviously behind the peak stress, which indicates that the permeability evolution characteristics have a significant lag effect compared with the stress-strain curve. The bedded sandstone under other working conditions has similar permeability evolution characteristics.

3.5.1. Permeability vs. confining pressure effect

To further obtain the law for the effect of confining pressure on the permeability evolution characteristics, the stress-permeability curves (k vs. σ_3) of bedded sandstone under H-M coupling are drawn (see Fig. 12). The permeability of bedded sandstone showed similar evolution trends under different working conditions. With increasing confining pressure, the permeability under identical bedding angle and identical axial stress level decreased significantly. The radial constraint effect was significantly enhanced with increasing confining pressure, which inhibited internal radial cracks and compacted them. Therefore, the opening of its internal dominant seepage channel became decreased, finally forming an objective law that the permeability gradually decreased with the increase in confining pressure.

The fitting curves of the initial permeability k_0, minimum permeability k_{min}, final permeability k_{fin} and confining pressure are shown in Fig. 13. As shown in Fig. 13a, the initial permeability with identical bedding angle showed a significant negative linear relationship with the increase in confining pressure, while the initial permeability with identical confining pressure increased as bedding angle increased. As shown in Fig. 13b, the minimum permeability showed a significant negative linear relationship with increasing confining pressure, while the minimum permeability with medium/high confining pressures increased as the bedding angle increased. However, the minimum permeability under low confining pressure decreased first and then increased as the bedding angle increased. Similarly, the final permeability also presented a significant negative linear relationship with increasing confining pressure. In addition, the final permeability increased as the bedding angle increased (see Fig. 13c). Moreover, the correlation coefficients R^2 of the above fitting functions were close to 1, which also indicated that the confining pressure had an obvious effect on the initial, minimum and final permeabilities.

3.5.2. Permeability vs. bedding effect

To further obtain the anisotropic evolution law of permeability, the stress-permeability curve (k vs. β) is plotted (see Fig. 14). The

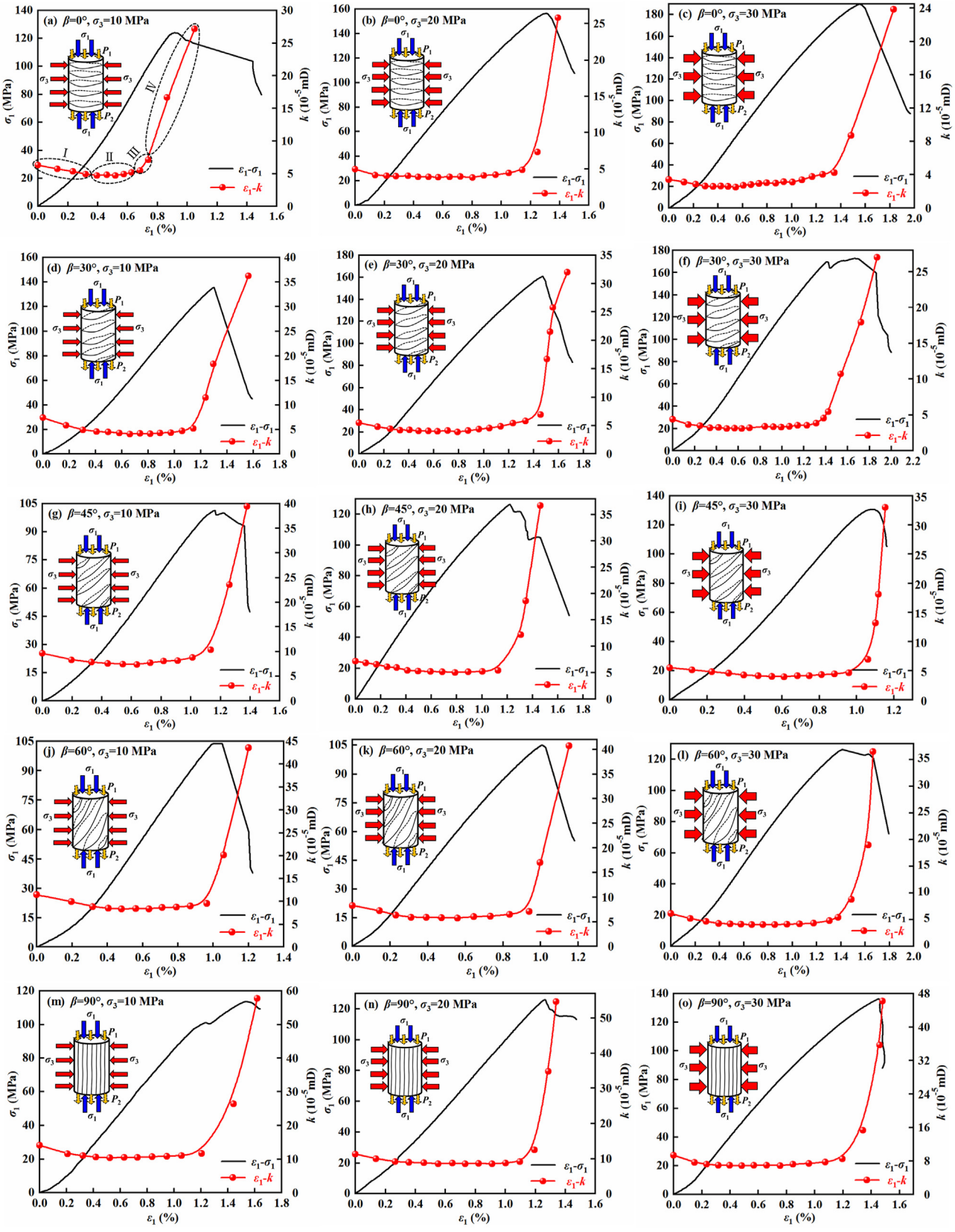

Fig. 11. Stress-strain-permeability curves under H-M coupling.

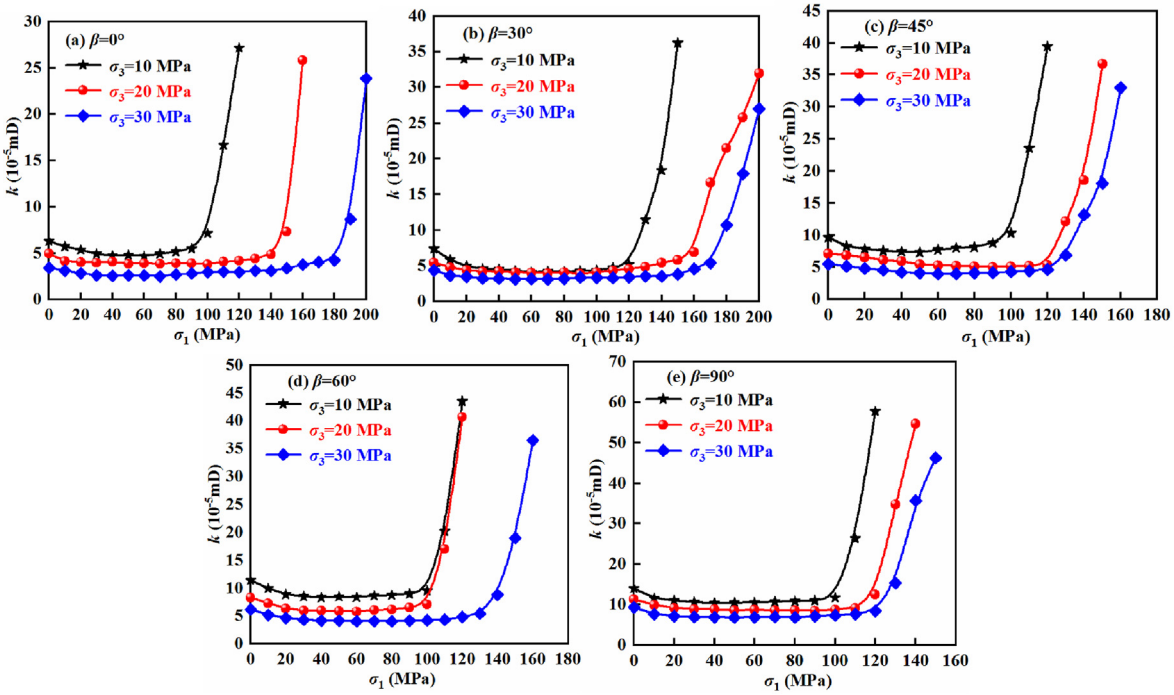

Fig. 12. Stress-permeability curves under H-M coupling (k vs. σ_3).

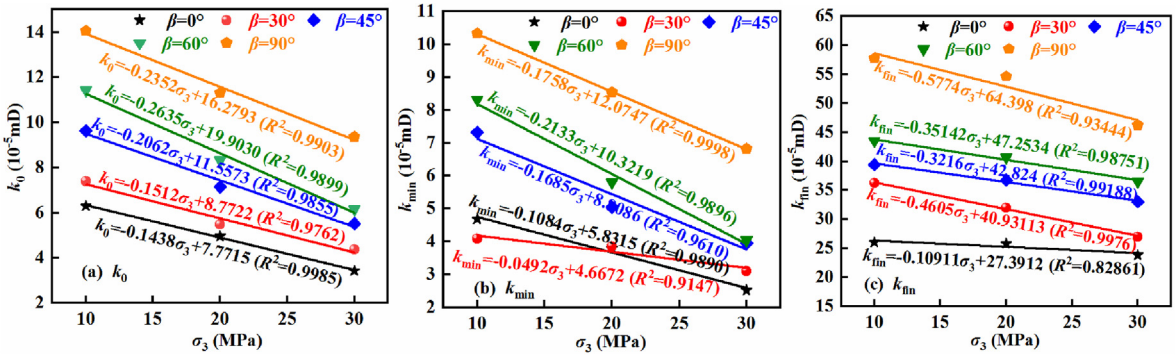

Fig. 13. Fitting curves of the characteristic permeability and confining pressure under H-M coupling.

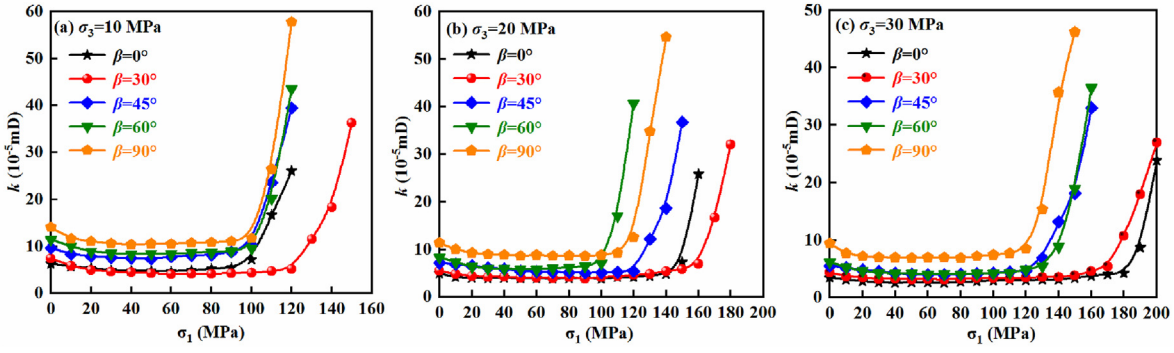

Fig. 14. Stress-permeability curves under H-M coupling (k vs. β).

permeability with identical confining pressure and axial stress level increased with increasing bedding angle. Particularly, the bedded sandstone with the bedding angle of 0° had the minimum permeability, while that with the bedding angle of 90° had the maximum permeability. Increasing bedding angle could greatly shorten the equivalent length of the effective seepage path. An

increase in the effective seepage path length significantly reduced the permeability. That is, under the action of effective stress, the dominant seepage channel formed was close to the same direction as the water seepage, which led to the maximum permeability of the bedded sandstone containing the weak plane of 90°. Therefore, the structures of the weak plane of 90° played a leading role. However, under the bedding angle of 0°, the formation of seepage channels depended on the orientation, length and number of cracks that broke down the matrix under the comprehensive action of effective stress. According to the Griffith's strength theory, compared with well-developed structures of bedding planes, it was more difficult to break down the matrix to produce more cracks, and the ability to form dominant seepage channels was also the weakest. Therefore, the permeability with the bedding angle of 0° was the smallest.

The fitting curves of the initial permeability k_0, minimum permeability k_{min}, final permeability k_{fin} and bedding angle are shown in Fig. 15. With the increase in bedding angle, the initial permeability with identical confining pressure showed a significant positive linear relationship (see Fig. 15a). Meanwhile, the initial permeability with identical bedding angle decreased with the increase in confining pressure. The minimum permeability showed an obvious positive nonlinear relationship with increasing bedding angle (see Fig. 15b). However, the minimum permeability curve with the bedding angle of 30° under the confining pressure of 10 MPa showed a sudden drop, which was caused by the different internal structural states, resulting in certain differences in the closure mode and state of cracks. Similarly, the final permeability also presented a significant positive nonlinear relationship with increasing bedding angle (see Fig. 15c). Meanwhile, the final permeability under identical bedding angle decreased with the increase in confining pressure. The correlation coefficients R^2 of the above fitting functions were close to 1, which also demonstrated that the bedding angle had an obvious effect on the initial, minimum and final permeabilities.

3.5.3. Permeability vs. coupling effect

As shown in Fig. 16a–c, evolution models of the initial, minimum and final permeability were established. Among them, the initial permeability, minimum permeability, final permeability, bedding angle and confining pressure all showed a significant binary primary function relationship. Additionally, the correlation coefficients R^2 of the above fitting functions were close to 1, which indirectly verified the rationality of the characteristic permeability evolution models established.

Furthermore, the combination of low confining pressure and bedding angle of 90° parallel to the seepage direction led to the largest initial permeability and minimum permeability (see Fig. 16d–e). It also indicated that the effects of the confining pressure and bedding had significant influences on the evolution characteristics of the initial, minimum and final permeabilities. However, the bedding angle had slightly weaker influences on the initial, minimum and final permeabilities than that of confining pressure.

3.6. Damage evolution characteristics

AE parameters can effectively characterize the mechanical behaviours of bedded sandstone, such as the closure, compaction, damage propagation and complete failure of internal microcracks. Under the continuous action of external loads, the internal cracks of bedded sandstone can experience a series of changes. In this process, the elastic wave can be released, and the AE can effectively monitor the whole process. Therefore, it can better reflect the progressive failure characteristics of bedded sandstone. Therefore, the ringing count was used as one of the parameters of AE nondestructive monitoring. Among them, the relationship curve of the stress-strain-ringing count under H-M coupling is shown in Fig. 17.

The stress-strain-ringing count N_t relation curves of bedded sandstone had significant similarities (see Fig. 17). Therefore, Fig. 17a was selected to give a representative description of the ringing count evolution characteristics during the whole deformation process.

At initial crack compaction stage I, the bedded sandstone was subjected to the continued actions of effective stresses, the internal primary cracks closed, and the ringing count increased slightly (see Fig. 17).

However, when it transferred to linear elastic deformation stage II, the ringing count distribution characteristics were mainly sporadic with generally small values. At this stage, the bedded sandstone was close to the elastic body, and the initial primary cracks were almost compressed, but the weak slipping between the bedding interfaces could also produce weak elastic wave signals.

When entering crack stable growth stage III, the ringing count gradually increased, which corresponded to the new crack derivatives, stable growth and development at this stage.

When entering unstable crack growth stage IV, the ringing count started to increase sharply, the growth rate was obvious, and the ringing count reached the maximum at the peak strength. This result indicated that new cracks expanded → nucleation → the macroscopic and mesoscopic fractures formed at the peak strength.

When entering post-peak strain softening stage V, the bedded sandstone still had a certain bearing capacity. Meanwhile, the broken particles in its macroscopic fracture surfaces would have

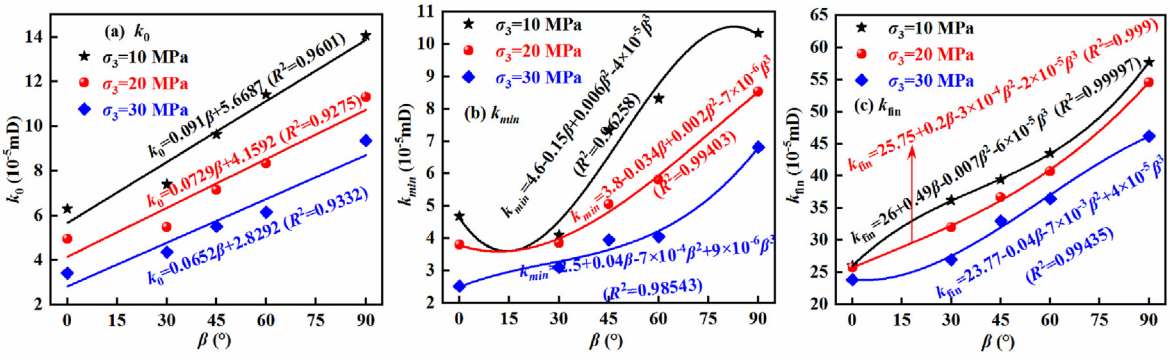

Fig. 15. Fitting curves of the characteristic permeability and bedding angle under H-M coupling.

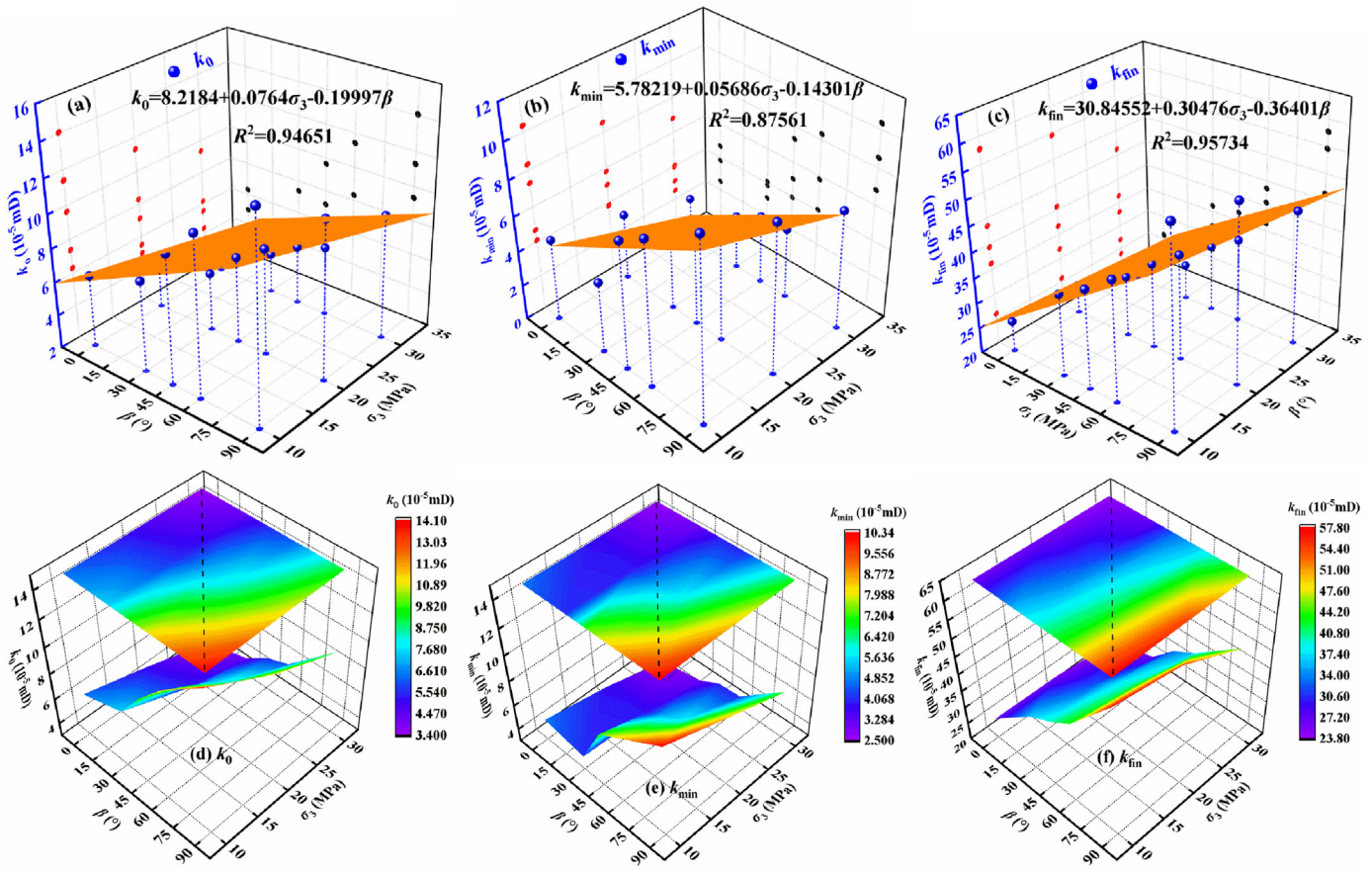

Fig. 16. Relationships between the characteristic permeability and coupling effect (bedding angle and confining pressure) under H-M coupling.

the mechanical behaviour characteristics of secondary particle breakage under the continuous extrusion of external loads. Therefore, the ringing count at this stage drops sharply, leaving only some signals or even no signal of the external characteristics.

Compared with the radial inhibition of medium and low confining pressures, the radial inhibition of high confining pressure is more significant and effective. Therefore, the existence of high confining pressure can more effectively inhibit the growth and development of internal cracks in bedded sandstone. Then, it can effectively reduce the occurrence frequency and number of internal microcracks, thus effectively reducing the value of the ringing count. Therefore, compared with the maximum ringing count with identical bedding angle at high confining pressure, that at medium or low confining pressures was obviously higher.

The damage D is defined by the cumulative ringing count values:

$$D = \frac{C_t}{C_a} \tag{2}$$

where C_t and C_a are the cumulative ringing count values during initial loading and complete fracture, respectively.

Therefore, the stress-strain-damage relationship curve under H-M coupling is plotted (see Fig. 18). The damage evolution curve had a certain similarity with the ringing count evolution curve. In addition, there were four stages in the damage evolution curve: initial damage stage I, damage slowly increasing stage II, damage rapidly increasing stage III, and damage stable development stage IV. Among them, the proportion of total damage evolution in stage III is the largest and that at stage I or stage IV is the smallest.

At the initial damage stage I (corresponding to the initial crack compaction stage), the damage was less, and the value was lower. This was mainly due to the initial crack compaction in the bedded sandstone.

At the damage slowly increasing stage II (corresponding to the linear elastic deformation stage and crack stable growth stage), the damage gradually increased, and the value also increased. This was mainly due to the gradual emergence of numerous microcracks in bedded sandstone, and continuous penetration or slipping friction between bedding interfaces, which led to the gradual accumulation and increase in damage.

At the damage rapidly increasing stage III (corresponding to the unstable crack growth stage), the damage increased sharply. This was mainly due to the rapid expansion, growth and nucleation of numerous new microcracks in bedded sandstone and the formation of the macroscopic fracture surface at the peak strength, which led to the maximum damage at the peak strength.

At the damage stable development stage IV (corresponding to the post-peak strain softening stage), the damage was basically stable.

In addition, the evolution curve at the slow damage stage was longer as increasing confining pressure. It was suggested that the confining pressure played a leading role in inhibiting microcrack growth in bedded sandstone compared with the bedding effect at this stage.

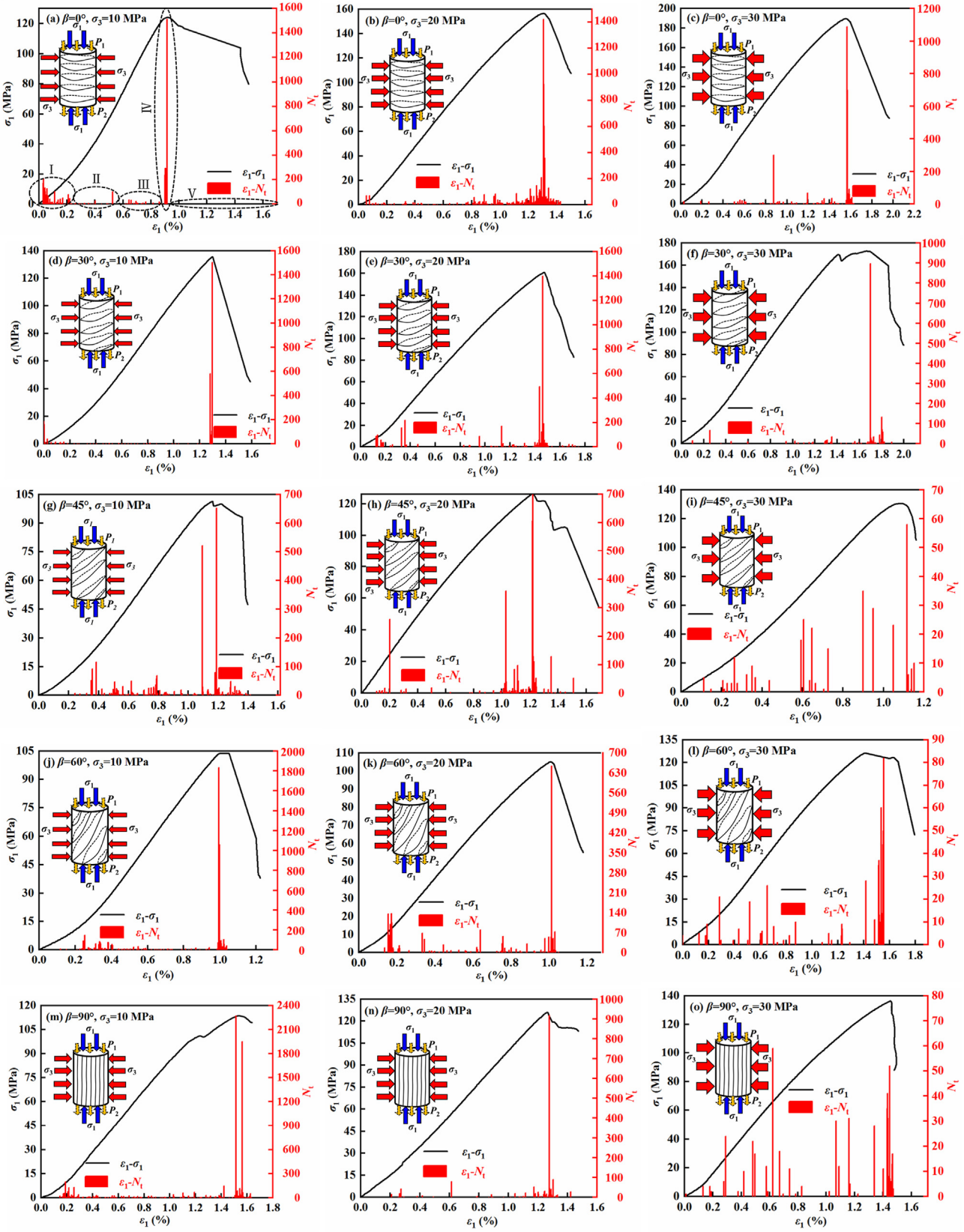

Fig. 17. Stress-strain-ring count curves under H-M coupling.

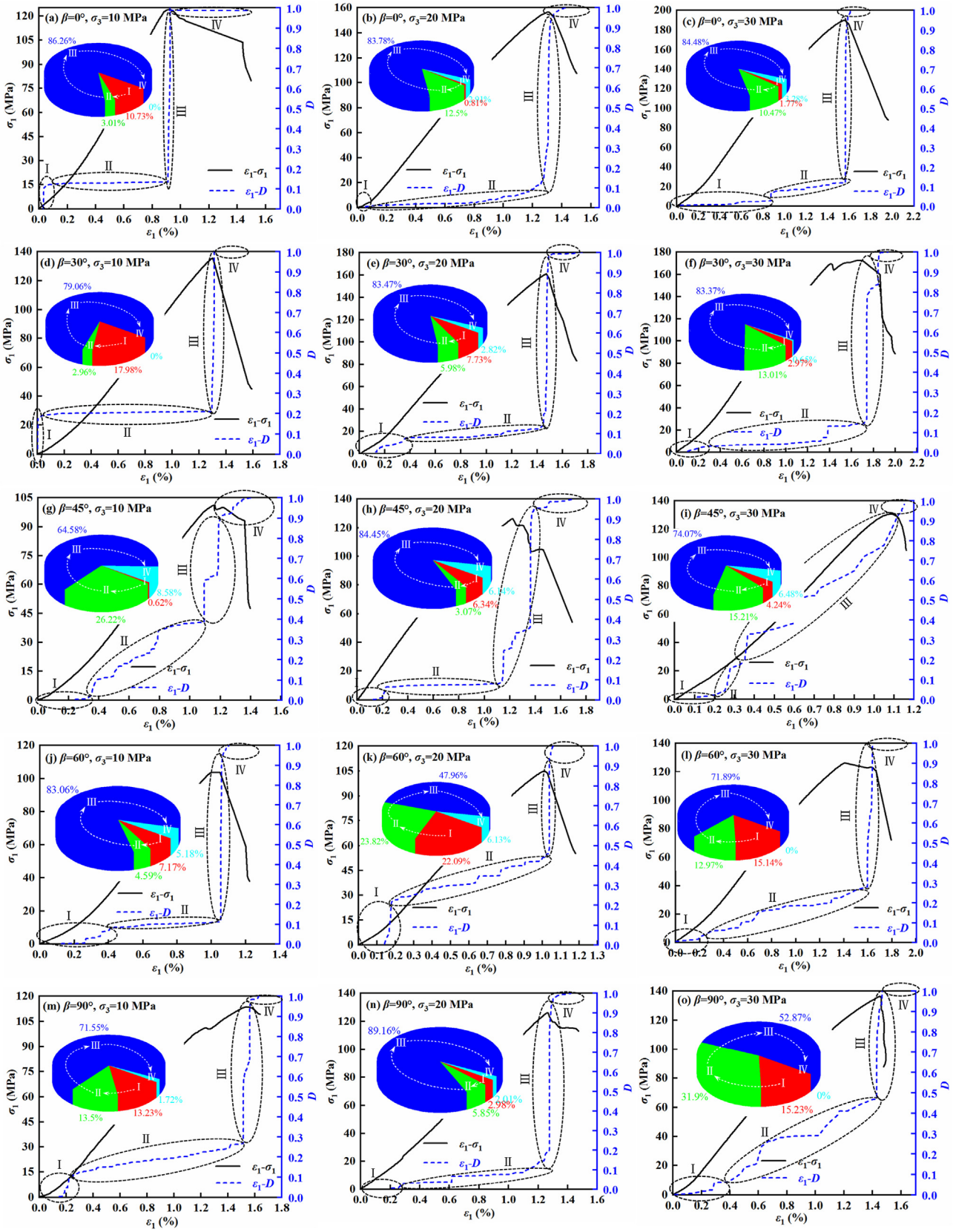

Fig. 18. Stress-strain-damage evolution curves under H-M coupling.

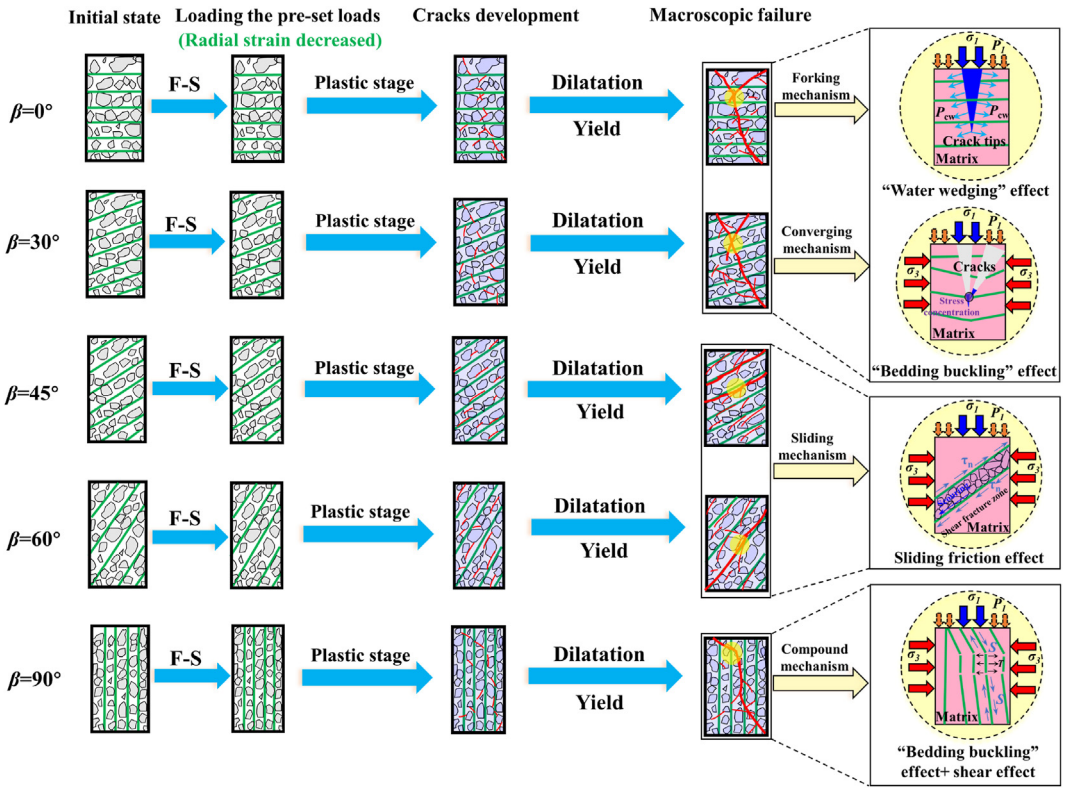

Fig. 19. Failure mechanism under H-M coupling. Note: F–S represents the state of H-M coupling; β is the bedding angle; P_{cw} is the pore water pressure at the crack tips; σ_1, σ_3 and P_1 represent the axial pressure, confining pressure and inlet pressure, respectively; and S, T and τ_n represent the shear stress, tensile stress and tangential stress, respectively.

3.7. *Failure mechanism*

Based on the above analysis, the failure mechanism of bedded sandstone under H-M coupling was further revealed. The details of the failure mechanism under various bedding angles are shown in Fig. 19. The bedded sandstones with various bedding angles experienced an evolution process in which the radial strain decreased, the crack developed, propagated and even entered the yield status (see Fig. 19). However, due to the comprehensive actions of the bedding effect, the effect of confining pressure and the effect of osmotic pressure eventually led to forming macroscopic failure characteristics with different forms.

Among them, due to the existence of the "water wedging" effect (Deng et al., 2017), the macroscopic and mesoscopic fracture characteristics of shear failure through the bedding plane in forking with bedding angles of 0° and 30° were formed. Because the pore water pressure of seepage water could make the internal crack tips form the secondary fracture, which could make its forking occur in the crack tips. That is, the corresponding seepage water in the crack tips played a role that was similar to the wedge "medium". However, due to the existence of the "bedding buckling" effect, the macro- and mesoscopic fracture characteristics of shear failure with the bedding plane converging under bedding angles of 0° and 30° were formed. The reason was mainly that the angle between the confining pressure and the weak bedding plane was relatively small, which easily led to a weak bedding plane with low cohesion producing the small-angle "bending" phenomenon in the horizontal direction. Meanwhile, a stress concentration was easily formed at the "bending" tips, which could effectively induce the mechanical behaviours such as extension, expansion and convergence of microcracks at multiple places, and finally form the macro- and mesoscopic fracture characteristics of shear failure in convergence.

The macroscopic and mesoscopic fracture characteristics of shear slipping failure along the bedding plane under bedding angles of 45° and 60° were formed. Due to the existence of the sliding friction effect, leading to the formation of a shear fracture zone under bedding angles of 45° and 60°. Meanwhile, the broken particles in the shear fracture zone were easily washed away by the seepage water under H-M coupling.

The characteristics of mixed failure through the bedding plane under the bedding angle of 90° were formed. This was mainly due to the combination of the "bedding buckling" effect and shear effect. Because the bedding weak plane of 90° was parallel to the axial stress, it was easy to form the "bedding buckling" phenomenon on the weak plane under continuous actions of high effective stresses. Meanwhile, the local shear zone is easily formed under the bedding angle of 90°, which led to local shear failure. Therefore, the failure mechanism of bedded sandstone with a bedding angle of 90° could be clarified.

4. Conclusions

In this paper, the H-M coupling experiments under various bedding angles, identical osmotic pressure and various confining pressures were systematically conducted. The mechanical behaviors of bedded sandstone with various bedding angles under H-M coupling were also quantitatively characterized, including the strength, deformation, permeability, damage, macro- and microscopic failure characteristics. Finally, the failure mechanism of bedded sandstone with various bedding angles under H-M

coupling was revealed. The following conclusions can be drawn as follows:

(1) The combination of bedding angle and effective stress results in different macroscopic failure modes of bedding sandstones with various bedding angles. Among them, due to a certain angle between the direction of effective stress and the beddings of 0° and 30°, the macroscopic failure type with the bedding angles of 0° and 30° was shear failure through the bedding plane; Nevertheless, due to the direction of effective stress was basically parallel to the bedding angles of 45° or 60°, their macroscopic failure type was mainly shear failure along the bedding plane; When the bedding angle was 90° (which was parallel to the loading direction of axial stress and perpendicular to the loading direction of confining pressure), the macroscopic failure modes with bedding angle of 90° was mainly the mixed tension-shear failure.
(2) Within $\beta \in (0°, 30°)$ and $\beta \in (45°, 90°)$, the confining pressure played a more dominant role on influencing the peak deviatoric stress than that of the bedding angle. Nevertheless, within $\beta \in (30°, 45°)$, the bedding angle played a more dominant role in influencing the peak deviatoric stress than that of the confining pressure.
(3) Corresponded to the bedding angles of 0°, 30°, 45°, 60° and 90°, the cohesions were 25.7947 MPa, 46.6397 MPa, 39.1187 MPa, 27.7762 MPa and 38.6679 MPa, respectively. Meanwhile, the corresponding internal friction angles were 44.1123°, 17.3071°, 17.9839°, 29.4466° and 19.1136°, respectively.
(4) The permeability under identical confining pressure and axial stress level increased as the bedding angle increases. Nevertheless, under the same confining pressure, the minimum permeability showed a significant negative linear relationship with the increase in bedding angle.
(5) The "water wedging" effect and the "bedding buckling" effect resulted in the shear failure through the bedding plane in forking and convergence formed under bedding angles of 0° and 30°, respectively. Additionally, the sliding friction effect led the bedded sandstone with bedding angles of 45° and 60° forming the shear slipping failure along the bedding plane. Finally, due to the combination of the "bedding buckling" effect and shear effect, the failure characteristics of the mixed tension-shear failure through the bedding plane under the bedding angle of 90° was formed.

Declaration of competing interest

The authors declare that they have no known competing financial interests or personal relationships that could have appeared to influence the work reported in this paper.

Acknowledgments

This study was supported by the National Natural Science Foundation of China (Grant Nos. 52034009 and 51974319) and the Yue Qi Distinguished Scholar Project (Grant No. 2020JCB01).

References

Chen, D., Pan, Z., Liu, J., Connell, L., 2012. Modeling and simulation of moisture effect on gas storage and transport in coal seams. Energy Fuel. 26, 1695–1706.
Chen, H., Cheng, Y., Zhou, H., 2013. Damage and permeability development in coal during unloading. Rock Mech. Rock Eng. 46 (3), 1377–1390.
Deng, H.F., Wang, Z., Li, J.L., Jiang, Q., Zhang, H.B., 2017. Experimental research about influence of low pore water pressure on unloading mechanical properties of sandstone. Chin. J. Rock Mech. Eng. 36 (S1), 3266–3275.
Han, F., Busch, A., Wageningen, N., Yang, J., Liu, Z., Krooss, B., 2010. Experimental study of gas and water transport processes in the inter-cleat (matrix) system of coal: anthracite from Qinshui Basin, China. Int. J. Coal Geol. 81 (2), 128–138.
Hu, M.S., Wang, Y., Rutqvist, J., 2017. Fully coupled hydro-mechanical numerical manifold modeling of porous rock with dominant fractures. Acta. Geotech. 12 (2), 231–252.
Izadi, G., Wang, S., Elsworth, D., Liu, J., Wu, Y., Pone, D., 2011. Permeability evolution of fluid-infiltrated coal containing discrete fractures. Int. J. Coal Geol. 85 (2), 202–211.
Jiang, Z.M., Feng, S.R., Fu, S., 2012. Coupled hydro-mechanical effect of a fractured rock mass under high water pressure. J. Rock. Mech. Geotech. 4 (1), 88–96.
Kang, H.P., 2021. Temporal scale analysis on coal mining and strata control technologies. J. Min. Strata. Control. Eng. 3 (1), 5–27.
Le, A.D., Nguyen, T.S., 2015. Hydromechanical response of a bedded argillaceous rock formation to excavation and water injection. Can. Geotech. J. 52 (1), 1–17.
Lei, H., Xu, T., Jin, G., 2015. TOUGH2Biot-a simulator for coupled thermal-hydrodynamic-mechanical processes in subsurface flow systems: application to CO_2 geological storage and geothermal development. Comput. Geosci. 77, 8–19.
Li, Z., Nguyen, S., Su, G., Labrie, D., Barnichon, J.D., 2017. Development of a viscoelastoplastic model for a bedded argillaceous rock from laboratory triaxial test. Can. Geotech. J. 54 (3), 359–372.
Maruvanchery, V., Kim, E., 2020. Effects of a high temperature (500°C) on the fracture processes in calcite-cemented sandstone along bedding-plane orientations. Rock Mech. Rock Eng. 53 (2), 955–966.
Morris, J.P., Hao, Y., Foxall, W., McNab, W., 2011. In Salah CO_2 Storage JIP: hydro-mechanical simulations of surface uplift due to CO_2 injection at in Salah. Energy Proc. 4, 3269–3275.
Ng, K., Carlos Santamarina, J., 2023. Mechanical and hydraulic properties of carbonate rock: the critical role of porosity. J. Rock. Mech. Geotech. 15 (4), 814–825.
Nguyen, T.S., Li, Z.Z., Su, G., Nasseri, M.H.B., Young, R.P., 2018. Hydro-mechanical behavior of an argillaceous limestone considered as a potential host formation for radioactive waste disposal. J. Rock. Mech. Geotech. 10 (6), 59–77.
Pan, Z., Connell, L., Camilleri, M., Connelly, L., 2010. Effects of matrix moisture on gas diffusion and flow in coal. Fuel 89 (11), 3207–3217.
Perera, M., Ranjith, P., Peter, M., 2011. Effects of saturation medium and pressure on strength parameters of Latrobe Valley brown coal: carbon dioxide, water and nitrogen saturations. Energy 36 (12), 6941–6947.
Poulsen, B., Shen, B., Williams, D., Huddlestone-Holmes, C., Erarslan, N., Qin, J., 2014. Strength reduction on saturation of coal and coal measures rocks with implications for coal pillar strength. Int. J. Rock Mech. Min. Sci. 71, 41–52.
Ren, C., Li, B., Xu, J., Zhang, Y., Li, J., Gao, Z., Yu, J., 2020. A novel damage-based permeability model for coal in the compaction and fracturing process under different temperature conditions. Rock Mech. Rock Eng. 53, 5697–5713.
Rutqvist, J., Liu, H.H., Vasco, D.W., Pan, L., Kappler, K., Majer, E., 2011. Coupled non-isothermal, multiphase fluid flow, and geomechanical modeling of ground surface deformations and potential for induced micro-seismicity at the in Salah CO_2 storage operation. Energy Proc. 4 (1), 3542–3549.
Su, R.H., Liu, X.L., 2020. Fracture failure characteristics of jointed sandstone under uniaxial compression. Geofluids 1–14, 2020.
Song, Z.X., Zhang, J.W., Dong, X.K., Zhang, Y., Zhang, Y.J., An, S., 2022. Time-dependent behaviors and volumetric recovery phenomenon of sandstone under triaxial loading and unloading. J. Cent. South. Univ. 29 (12), 4002–4020.
Song, Z.X., Zhang, J.W., 2022. Research on the progressive failure process and fracture mechanism of rocks with the structural evolution perspective. J. Struct. Geol. 154, 104484.
Song, Z.X., Zhang, J.W., Wang, S.Y., Dong, X.K., Zhang, Y., 2023a. Energy evolution characteristics and weak structure - "energy flow" impact damaged mechanism of deep-bedded sandstone. Rock Mech. Rock Eng. 56 (3), 2017–2047.
Song, Z.X., Zhang, J.W., Wu, S.K., 2023b. Energy dissipation and fracture mechanism of layered sandstones under coupled hydro-mechanical unloading. Processes 11, 2041.
Song, Z.X., Zhang, J.W., Zhang, Y., Dong, X.K., Wang, S.Y., 2023c. Characterization and evaluation of brittleness of deep bedded sandstone from the perspective of the whole life-cycle evolution process. Int. J. Min. Sci. Technol. 33 (4), 481–502.
Vishal, V., Ranjith, P., Singh, T., 2015. An experimental investigation on behaviour of coal under fluid saturation, using acoustic emission. J. Nat. Gas Sci. Eng. 22, 428–436.
Wang, W., Kosakowski, G., Kolditz, O., 2009. A parallel finite element scheme for thermo-hydro-mechanical (THM) coupled problems in porous media. Comput. Geosci. 35 (8), 1631–1641.
Wang, S., Elsworth, D., Liu, J., 2011. Permeability evolution in fractured coal: the roles of fracture geometry and water-content. Int. J. Coal Geol. 87 (1), 13–25.
Wang, Z.H., Li, B.B., Ren, C.H., Xu, J., Gao, Z., Zhang, Y., 2022. A permeability model for coal based on elastic and plastic deformation conditions under the interaction of hydro-mechanical effects. J. Petrol. Sci. Eng. 212, 110209.
Watanabe, N., Wang, W., McDermott, C.I., Taniguchi, T., Kolditz, O., 2010. Uncertainty analysis of thermo-hydro-mechanical coupled processes in heterogeneous porous media. Comput. Mech. 45 (4), 263–280.

Wu, G.J., Jia, S.P., Wu, B.L., 2019. Comparison of a novel coupled hydro-mechanical model with typical analytical models in subsidence of coal seam gas extraction. Int. J. Oil Gas Coal Technol. 22 (2), 246–268.
Yan, B.Q., Kang, H.P., Li, X.S., Qi, Q.J., Zhang, B., Liu, J.Z., 2023. Damage constitutive model and mechanical properties of jointed rock mass under hydro-mechanical coupling. Theor. Appl. Fract. Mech. 123, 103735.
Yu, M.Y., Liu, B.G., Chu, Z.F., Sun, J.L., Deng, T.B., Wang, Q., 2022. Permeability, deformation characteristics, and damage constitutive model of shale under triaxial hydromechanical coupling. Bull. Eng. Geol. Environ. 81 (3), 85.
Zhao, Y., Du, C., Bi, J., Wang, C.L., 2021. Experimental investigation of triaxial compression and permeability of gritstone in geothermal environment. Bull. Eng. Geol. Environ. 80 (9), 6971–6988.
Zhang, J.W., Song, Z.X., Wang, S.Y., 2021. Experimental investigation on permeability and energy evolution characteristics of deep sandstone along a three-stage loading path. Bull. Eng. Geol. Environ. 80 (2), 1571–1584.
Zheng, H., Cao, S.Q., Yuan, W., Jiang, Q., Li, S.J., Feng, G.L., 2022. A time-dependent hydro-mechanical coupling model of reservoir sandstone during CO_2 geological storage. Rock Mech. Rock Eng. 55, 5845–5861.
Zhou, J.R., Lou, J.F., Wei, J., Dai, F., Chen, J.K., Zhang, M.S., 2023. A 3D microseismic data-driven damage model for jointed rock mass under hydro-mechanical coupling conditions and its application. J. Rock. Mech. Geotech. 15 (4), 911–925.
Zhu, W., Wei, C., 2011. Numerical simulation on mining-induced water inrushes related to geologic structures using a damage-based hydromechanical model. Environ. Earth Sci. 62 (1), 43–54.

Junwen Zhang is professor, doctoral supervisor, visiting scholar of the University of Newcastle in Australia funded by the China Scholarship Council, and associate head of the School of Energy and Mining Engineering, China University of Mining and Technology (Beijing). He is mainly engaged in the research of deep coal mining methods, rockburst prevention, combined disaster prevention of the coal, rock and gas, mine pressure and ground control, roadway surrounding rock stability control of roadways. He hosted more than ten research projects, including the key national natural science foundation funding, the joint key funding of the national science foundation and enterprise innovation development. As the first author/corresponding author, he published more than 70 papers indexed by SCI/EI. He has won the Coal Youth Science and Technology Award and the Green Mine Outstanding Contribution Award.